



HAL
open science

Discovery of a Damped Ly α Absorber Originating in a Spectacular Interacting Dwarf Galaxy Pair at $z = 0.026$

Erin Boettcher, Neeraj Gupta, Hsiao-Wen Chen, Mandy C. Chen, Gyula I. G. Józsa, Gwen C. Rudie, Sebastiano Cantalupo, Sean D. Johnson, S. A. Balashev, Françoise Combes, et al.

► To cite this version:

Erin Boettcher, Neeraj Gupta, Hsiao-Wen Chen, Mandy C. Chen, Gyula I. G. Józsa, et al.. Discovery of a Damped Ly α Absorber Originating in a Spectacular Interacting Dwarf Galaxy Pair at $z = 0.026$. The Astrophysical journal letters, 2022, 926, 10.3847/2041-8213/ac5250 . insu-03717132

HAL Id: insu-03717132

<https://insu.hal.science/insu-03717132>

Submitted on 9 Jul 2022

HAL is a multi-disciplinary open access archive for the deposit and dissemination of scientific research documents, whether they are published or not. The documents may come from teaching and research institutions in France or abroad, or from public or private research centers.

L'archive ouverte pluridisciplinaire **HAL**, est destinée au dépôt et à la diffusion de documents scientifiques de niveau recherche, publiés ou non, émanant des établissements d'enseignement et de recherche français ou étrangers, des laboratoires publics ou privés.



Distributed under a Creative Commons Attribution 4.0 International License



Discovery of a Damped Ly α Absorber Originating in a Spectacular Interacting Dwarf Galaxy Pair at $z = 0.026$

Erin Boettcher^{1,2,3} , Neeraj Gupta⁴ , Hsiao-Wen Chen³ , Mandy C. Chen³ , Gyula I. G. Józsa^{5,6,7} , Gwen C. Rudie⁸ , Sebastiano Cantalupo⁹ , Sean D. Johnson¹⁰ , S. A. Balashev^{11,12} , Françoise Combes¹³ , Kathy L. Cooksey¹⁴ , Claude-André Faucher-Giguère¹⁵ , Jens-Kristian Krogager¹⁶ , Sebastian Lopez¹⁷ , Emmanuel Momjian¹⁸ , Pasquier Noterdaeme^{19,20} , Patrick Petitjean¹⁹ , Marc Rafelski^{21,22} , Raghunathan Srianand⁴ , Gregory L. Walth⁸ , and Fakhri S. Zahedy⁸ 

¹ Department of Astronomy, University of Maryland, College Park, MD 20742, USA; eboettch@umd.edu

² Code 662, NASA Goddard Space Flight Center, Greenbelt, MD 20771, USA

³ Department of Astronomy & Astrophysics, The University of Chicago, 5640 South Ellis Avenue, Chicago, IL 60637, USA

⁴ Inter-University Centre for Astronomy and Astrophysics, Post Bag 4, Ganeshkhind, Pune 411 007, India

⁵ South African Radio Astronomy Observatory, 2 Fir Street, Black River Park, Observatory, Cape Town, 7925, South Africa

⁶ Department of Physics and Electronics, Rhodes University, P.O. Box 94, Makhanda, 6140, South Africa

⁷ Max-Planck-Institut für Radioastronomie, Radioobservatorium Effelsberg, Max-Planck-Straße 28, 53902 Bad Münstereifel, Germany

⁸ The Observatories of the Carnegie Institution for Science, 813 Santa Barbara Street, Pasadena, CA 91101, USA

⁹ Department of Physics, University of Milan Bicocca, Piazza della Scienza 3, I-20126 Milano, Italy

¹⁰ Department of Astronomy, University of Michigan, Ann Arbor, MI 48109, USA

¹¹ Ioffe Institute, Politekhnicheskaya 26, 194021 Saint Petersburg, Russia

¹² HSE University, Saint Petersburg, Russia

¹³ Observatoire de Paris, LERMA, Collège de France, CNRS, PSL University, Sorbonne University, F-75014 Paris, France

¹⁴ Department of Physics and Astronomy, University of Hawai'i at Hilo, Hilo, HI 96720, USA

¹⁵ Department of Physics & Astronomy and Center for Interdisciplinary Exploration and Research in Astrophysics (CIERA), Northwestern University, 1800 Sherman Avenue, Evanston, IL 60201, USA

¹⁶ Department of Astronomy, University of Geneva, Chemin Pegasi 51, 1290 Versoix, Switzerland

¹⁷ Departamento de Astronomía, Universidad de Chile, Casilla 36-D, Santiago, Chile

¹⁸ National Radio Astronomy Observatory, P.O. Box O, Socorro, NM 87801, USA

¹⁹ Institut d'Astrophysique de Paris, CNRS-SU, UMR7095, 98bis Bd Arago, F-75014 Paris, France

²⁰ Franco-Chilean Laboratory for Astronomy, IRL 3386, CNRS and Departamento de Astronomía, Universidad de Chile, Casilla 36-D, Santiago, Chile

²¹ Space Telescope Science Institute, Baltimore, MD 21218, USA

²² Department of Physics & Astronomy, Johns Hopkins University, Baltimore, MD 21218, USA

Received 2021 December 7; revised 2022 February 3; accepted 2022 February 5; published 2022 February 23

Abstract

We present the discovery of neutral gas detected in both damped Ly α absorption (DLA) and HI 21 cm emission outside of the stellar body of a galaxy, the first such detection in the literature. A joint analysis between the Cosmic Ultraviolet Baryon Survey and the MeerKAT Absorption Line Survey reveals an HI bridge connecting two interacting dwarf galaxies ($\log(M_{\text{star}}/M_{\odot}) = 8.5 \pm 0.2$) that host a $z = 0.026$ DLA with $\log[N(\text{HI})/\text{cm}^{-2}] = 20.60 \pm 0.05$ toward the QSO J2339–5523 ($z_{\text{QSO}} = 1.35$). At impact parameters of $d = 6$ and 33 kpc, the dwarf galaxies have no companions more luminous than $\approx 0.05L_{*}$ within at least $\Delta v = \pm 300 \text{ km s}^{-1}$ and $d \approx 350$ kpc. The HI 21 cm emission is spatially coincident with the DLA at the 2σ – 3σ level per spectral channel over several adjacent beams. However, HI 21 cm absorption is not detected against the radio-bright QSO; if the background UV and radio sources are spatially aligned, the gas is either warm or clumpy (with a spin temperature to covering factor ratio $T_s/f_c > 1880$ K). Observations with VLT-MUSE demonstrate that the α -element abundance of the ionized interstellar medium (ISM) is consistent with the DLA ($\approx 10\%$ solar), suggesting that the neutral gas envelope is perturbed ISM gas. This study showcases the impact of dwarf–dwarf interactions on the physical and chemical state of neutral gas outside of star-forming regions. In the SKA era, joint UV and HI 21 cm analyses will be critical for connecting the cosmic neutral gas content to galaxy environments.

Unified Astronomy Thesaurus concepts: [Damped Lyman-alpha systems \(349\)](#); [Dwarf galaxies \(416\)](#); [H I line emission \(690\)](#); [Tidal interaction \(1699\)](#); [Interstellar medium \(847\)](#); [Interstellar line emission \(844\)](#); [Quasar absorption line spectroscopy \(1317\)](#); [Circumgalactic medium \(1879\)](#)

1. Introduction

Damped Ly α absorbers (DLAs; $\log[N(\text{HI})/\text{cm}^{-2}] \geq 20.3$) have sufficiently large HI column densities to be self-shielded against ionizing radiation and trace a dominant fraction of neutral gas in the universe, making them critical probes of the

galactic and circumgalactic environments related to star formation (for reviews, see Wolfe et al. 2005; Chen 2017; Krogager et al. 2017). Low-redshift DLAs ($z < 1$) detected through ultraviolet (UV) absorption-line spectroscopy using the unique capabilities of the Hubble Space Telescope (HST) are particularly important to our understanding of DLA host galaxies, which can be most easily detected and characterized in the local universe (e.g., Battisti et al. 2012; Neeleman et al. 2016; though note discussion of possible redshift evolution in the DLA host galaxy population, e.g., Neeleman et al. 2019;

Kaur et al. 2021). Previous studies suggest that low-redshift DLA host galaxies resemble the general field population and are thus diverse in their colors, luminosities, and environments, including both isolated galaxies and group members (e.g., Chen & Lanzetta 2003; Chen et al. 2005; Rao et al. 2011; Péroux et al. 2016).

Ambiguities in the origin of DLA gas—whether it is from a gaseous disk, a halo, intragroup gas, or infalling/outflowing material—can be understood by observing HI in emission through the 21 cm transition, which is sensitive to $N(\text{HI}) = \text{a few} \times 10^{18} \text{ cm}^{-2}$. If the background quasar is also bright at radio wavelengths, the HI 21 cm absorption can be used to constrain the cold neutral medium fraction of the DLA and the clumpiness of any cold gas (e.g., Srianand et al. 2012; Kanekar et al. 2014). However, DLAs in front of radio-loud quasars and at sufficiently low redshift ($z < 0.1$) to be detectable in HI 21 cm emission with current radio telescopes remain extremely rare.

Kanekar et al. (2018) reported HI 21 cm emission-line observations of four DLAs at $z < 0.1$, but the spatial resolution of these single-dish data is inadequate to unambiguously associate the 21 cm emission with individual galaxies or dissect its origin. To the best of our knowledge, only two cases of bona fide DLAs with spatially resolved HI 21 cm observations have been reported in the literature. In the first case, the quasar sight line passes through the optical extent of a low surface brightness galaxy at $z = 0.009$ (Bowen et al. 2001; Chengalur & Kanekar 2002). In the second case, Borthakur et al. (2019) mapped the neutral gas properties of a galaxy group that hosts a DLA at $z = 0.029$; no HI 21 cm emission was detected to be spatially coincident with the DLA. The quasar in both cases is not bright at radio wavelengths. The HI 21 cm emission-line detections of several galaxies associated with 21 cm absorbers have also been reported in the literature (e.g., Carilli & van Gorkom 1992; Dutta et al. 2016; Gupta et al. 2018). These confirm the complexity of the galaxy/absorber relationship, but UV-selected DLAs with spatially resolved HI 21 cm emission-line mapping of their galactic environments remain scarce.

Here we report the rare case of a bona fide DLA ($z = 0.026$) that coincides with HI 21 cm emission outside of the optical extent of a galaxy. The background QSO J2339–5523 ($z_{\text{QSO}} = 1.35$) is also bright at radio wavelengths (185 mJy at 1.4 GHz); thus, we can constrain the thermal state and clumpiness of the gas through HI 21 cm absorption. A deep galaxy redshift survey demonstrates that the DLA is associated with an interacting dwarf galaxy pair that is otherwise isolated from massive companions. This system is a valuable case study of the impact of dwarf–dwarf interactions on their neutral gas reservoirs independent of the influence of a nearby massive galaxy and its hot halo.

Throughout the paper, we adopt the solar abundance pattern of Asplund et al. (2009). We assume a Λ cosmology with $\Omega_M = 0.3$, $\Omega_\Lambda = 0.7$, and $H_0 = 70 \text{ km s}^{-1} \text{ Mpc}^{-1}$.

2. Data and Analysis

This study is based on data from the Cosmic Ultraviolet Baryon Survey (CUBS; Chen et al. 2020) and the MeerKAT Absorption Line Survey (MALS; Gupta et al. 2016). Below, we describe the data reduction and analysis of the UV absorption-line spectroscopy of J2339–5523 in Section 2.1, HI 21 cm observations from MeerKAT in Section 2.2, and optical integral field unit (IFU) observations from the Multi

Unit Spectroscopic Explorer (MUSE) on the Very Large Telescope (VLT) in Section 2.3.

2.1. UV Absorption-line Analysis

We refer the reader to Chen et al. (2020) for a description of the absorption-line observations of J2339–5523 from the Cosmic Origins Spectrograph (COS) on HST ($\lambda = 1100\text{--}1800 \text{ \AA}$, spectral resolution FWHM $\approx 20 \text{ km s}^{-1}$) and the Magellan Inamori Kyocera Echelle (MIKE) spectrograph on Magellan-Clay ($\lambda = 3200\text{--}9200 \text{ \AA}$, FWHM $\approx 8 \text{ km s}^{-1}$). We use Voigt profile fitting to determine the velocity (v), Doppler parameter (b), and column density (N) of the atomic and ionic transitions associated with the DLA using a grid search as described in Section 3 of Boettcher et al. (2021). The COS wavelength calibration is sufficiently uncertain that we allow small variations within $\delta v = \pm 5 \text{ km s}^{-1}$ for low and intermediate ions in COS with respect to Ca II $\lambda\lambda 3934, 3969$ in MIKE. We construct a marginalized probability density function for each parameter by calculating a likelihood of the form $\mathcal{L} \propto e^{-\chi^2/2}$ at every point in parameter space, normalizing the total likelihood to unity, and integrating over the marginalized parameters. We adopt as the best-fit model the parameters corresponding to a value of 50% from the cumulative distribution function. The reported uncertainties correspond to the 68% confidence interval, and the upper limits are reported as the 95% one-sided confidence interval. We additionally perform a curve-of-growth (COG) analysis for the low and intermediate ions to corroborate the characteristic Doppler parameter determined by the Voigt profile fitting.

2.2. MeerKAT HI 21 cm Analysis

We observed the field centered at J2339–5523 using the MeerKAT-64 array on 2020 June 14 and 22. Of the 64 antennas, 59 and 60 antennas participated in the first and second observing run, respectively. We used the 32K mode of the SKA Reconfigurable Application Board correlator to split the total bandwidth of 856 MHz centered at 1283.9869 MHz into 32,768 frequency channels. The resultant frequency resolution is 26.123 kHz, or 5.7 km s^{-1} , at the redshifted HI 21 cm line frequency of the DLA. Objects PKS 1939–638 and PKS 0408–658 were observed for flux density, delay, and bandpass calibrations, and the compact radio source J2329–4730 was observed for complex gain calibration. The total on-source time on J2339–5523 was 112 minutes.

The MeerKAT data were processed using the Automated Radio Telescope Imaging Pipeline; we refer the reader to Gupta et al. (2021) for details. Here we focus on the Stokes I radio continuum and spectral line properties near the HI 21 cm line frequency corresponding to $z_{\text{DLA}} (\sim 1384.4 \text{ MHz})$. The spatial resolution represented by the synthesized beam of the continuum image and image cube obtained using `robust = 0` weighting is $8''.4 \times 6''.6$ (position angle = $13^\circ 8$), with a spatial pixel size of $2''.0$. The cube has been deconvolved, or cleaned, using the CASA task `tclean` down to five times the single channel rms of $0.45 \text{ mJy beam}^{-1}$. The radio emission associated with J2339–5523 is compact with a deconvolved source size of $< 0''.6$.

We used the HI Source Finding Application (SOFIA v2.0; Serra et al. 2015; Westmeier et al. 2021) for the HI 21 cm analysis of the spectral line cube. We set SOFIA to subtract residual continuum subtraction errors from the image cube by

fitting a polynomial of order 1. We used the smooth+clip (S+C) algorithm with a combination of spatial kernels of zero, 3, 6, and 9 pixels and spectral kernels of zero, 3, 7, and 15 channels to detect voxels containing HI 21 cm emission in the image cube. We set the threshold of the S+C finder to 3.5σ and used the reliability filter to reject unreliable detections. The output three-dimensional mask was then used to further clean the image cube down to the single channel rms. This deep-cleaned cube was then passed through SOFIA with the abovementioned setup to generate the final HI moment maps and the integrated spectrum. For the moment 1 and 2 maps, we used only those pixels where the signal was detected at 1.5 times the local rms. In the moment zero map, the mean value of pixels with a signal-to-noise ratio (S/N) in the range 2.5σ – 3.5σ corresponds to an HI column density of $N(\text{HI}) = 3.2 \times 10^{20} \text{ cm}^{-2}$. This represents the average 3σ column density sensitivity across the map (see de Blok et al. 2018 for details of this sensitivity estimate).

2.3. VLT-MUSE Analysis

We observed the field of J2339–5523 on 2020 November 22, December 5, and December 9 using VLT-MUSE. The total exposure time on source was 9390 s. We reduced the data using the standard ESO MUSE pipeline (Weilbacher et al. 2014) and the custom software CubExtractor from S. Cantalupo (Cantalupo et al. 2019). We subtracted the quasar light using a high-resolution spectral differential imaging method (e.g., Haffert et al. 2019). The wavelength coverage is $\lambda = 4700$ – 9350 \AA , and the spectral resolution at the blue (red) end is $R \approx 1610$ ($R \approx 3570$). This corresponds to an FWHM of $\approx 185 \text{ km s}^{-1}$ (85 km s^{-1}), with approximately two wavelength bins sampling the spectral resolution element. Multiple pointings mapped a region of $1'3 \times 1'4$ around the QSO. We spatially smoothed the MUSE data cube with a boxcar kernel of 3×3 pixels, where the kernel size was chosen to approximate the seeing disk at the time of the observations ($\approx 0''.6$, or 0.3 kpc at the redshift of the DLA).

We construct continuum-subtracted narrowband images at the wavelength of all emission lines at the redshift of the DLA. We subtract the continuum by fitting a linear function locally around the masked lines. In parts of both dwarf galaxies, Balmer absorption from the stellar continuum modestly impacts the observed $\text{H}\alpha$ and $\text{H}\beta$ emission. To correct for this, we use the stellar population synthesis code *bagpipes*²³ (Carnall et al. 2018) to fit a tau model to the stellar continuum of a bright, star-forming region in each galaxy assuming a spatially uniform star formation history; the equivalent widths of the Balmer lines in the best-fit models are in the range 2.5 – 3.0 \AA . We then scale the models to the continuum level of any spaxel for which the continuum light is detected at $\geq 3\sigma$ at the wavelength of $\text{H}\alpha$ or $\text{H}\beta$. To allow for a possible velocity offset between the stars and the gas, we adopt a broad window of $\pm 500 \text{ km s}^{-1}$ ($\pm 180 \text{ km s}^{-1}$) when constructing the narrowband images of the Balmer lines for spaxels with (without) this correction applied. We derive an extinction correction using the extinction law of Cardelli et al. (1989) from the reddening, $E(B-V)$, calculated from the Balmer decrement following Calzetti et al. (1994) for every spaxel for which $\text{H}\beta$ and $\text{H}\alpha$ are detected at the $\geq 3\sigma$ level.

Finally, we fit the six strongest emission lines ($\text{H}\alpha$, $\text{H}\beta$, $[\text{O III}] \lambda\lambda 4960, 5008$, and $[\text{S II}] \lambda\lambda 6718, 6732$) with a single Gaussian profile using the IDL software KUBEVIZ.²⁴ This yields a velocity centroid and velocity dispersion, corrected for the instrumental resolution, for the ionized gas in each spaxel with statistically significant emission.

3. Results

We present the properties of the DLA in Section 3.1. We then discuss the associated dwarf galaxy pair in Section 3.2 before characterizing the neutral and warm ionized gas properties of the dwarfs and their environs in the following two sections.

3.1. A Dusty, Low-metallicity DLA

In Table 1, we list the best-fit column densities and Doppler parameters for all atomic and ionic species associated with the DLA, and we show a representative sample of the absorption lines and their best-fit models in Figure 1. The HI column density determined from the $\text{Ly}\alpha$ line is $\log[N(\text{HI})/\text{cm}^{-2}] = 20.60 \pm 0.05$. The uncertainty is dominated by the continuum fitting, as determined by repeated measurements of $N(\text{HI})$ from independent, manual fits to the local continuum prior to the $\text{Ly}\alpha$ fitting.

The Ca II $\lambda\lambda 3934, 3969$ lines are the only associated absorption features detected in the MIKE data and indicate a single velocity component at $z = 0.02604$, which we adopt as the velocity zero-point in the following analysis. The Ca II lines have a Doppler parameter of $b \approx 10 \text{ km s}^{-1}$, which we corroborate using a COG analysis for low and intermediate ions in COS that span a wide range of oscillator strengths. The best constraints come from six Fe II and six NI transitions; these measurements suggest that $10 \text{ km s}^{-1} \leq b \leq 20 \text{ km s}^{-1}$, and we impose this prior in the Voigt profile fitting of neutral, singly, and doubly ionized species. Only saturated or low-S/N lines are available for O I, C II, N II, Al II, Si II, and Si III, and we report a range of column densities corresponding to $10 \text{ km s}^{-1} \leq b \leq 20 \text{ km s}^{-1}$ for these species. There is some indication of moderate ionization state gas associated with the DLA from the detection of C IV (the Si IV transitions are contaminated by interlopers). The C IV Doppler parameter exceeds that of the low ions by a factor of 2, hinting that it may arise in a boundary layer between the neutral absorber and a hot ambient medium (e.g., Fox et al. 2005).

In panel (c) of Figure 1, we show the chemical abundances, $[X/H]$, for a range of elements ordered from most volatile to most refractory. Our best leverage on the metallicity of the DLA comes from S, which is only mildly depleted in a dusty medium (e.g., De Cia et al. 2016) and suggests $Z \approx 0.1Z_{\odot}$. In contrast, we find $[\text{Fe}/H] = -1.60 \pm 0.07$ and $[\text{Ca}/H] = -3.00 \pm 0.05$, suggesting dust depletion of the most refractory elements. The decrement in $[\text{Fe}/H]$ compared to $[\text{S}/H]$ is consistent with the Galactic halo depletion pattern of Savage & Sembach (1996). Due to the low second ionization energy of Ca (11.9 eV), it is possible that we underestimate $[\text{Ca}/H]$ by assuming $N(\text{Ca}) = N(\text{Ca II})$. However, the presence of dust depletion is clear from the underabundance of Fe alone. Applying the method of De Cia et al. (2021), we use the well-constrained S and Fe abundances to determine a total, dust-

²³ <https://bagpipes.readthedocs.io/en/latest/>

²⁴ <http://www.mpe.mpg.de/~dwilman/kubeviz/>

Table 1
 $z = 0.026$ DLA Properties

Column Densities for Limits and Ions Fit with b as a Free Parameter ^a			
Ion	b (km s ⁻¹)	log[N/cm ⁻²]	Comments
H I	...	20.60 ± 0.05	b unconstrained due to Ly α damping wings; N independent of b
C I	...	<13.4	b fixed to 10 km s ⁻¹ based on Ca II
C II*	...	<13.3	b fixed to 10 km s ⁻¹ based on Ca II
C IV	23 ⁺¹² ₋₈	13.45 ± 0.08	
N I	12 ± 2	14.46 ^{+0.05} _{-0.04}	
N V	...	<12.9	b fixed to 25 km s ⁻¹ based on C IV; comparable N found for $b \lesssim 100$ km s ⁻¹
Si IV	...	<13.0	b fixed to 25 km s ⁻¹ based on C IV; both 1393 and 1402 Å transitions contaminated
P II	...	12.9 ^{+0.1} _{-0.2}	Probability density function flat in b for 10 km s ⁻¹ ≤ b ≤ 20 km s ⁻¹
S II	10 ⁺² ₋₁	14.77 ^{+0.07} _{-0.05}	
S III	...	14.4 ± 0.1	S III λ 1190 blended with Si II λ 1190; S III b value not well constrained
Ca II	10.3 ^{+0.8} _{-0.7}	11.9 ± 0.02	
Fe II	14 ⁺⁴ ₋₃	14.55 ± 0.05	

Column Densities for $b = 10, 20$ km s ^{-1b}			
	log[N/cm ⁻²] ($b = 10$ km s ⁻¹)	log[N/cm ⁻²] ($b = 20$ km s ⁻¹)	
C II	17.6	15.1	C II λ 1334 is saturated
N II	14.7	14.2	Only low-S/N N II λ 1083 transition available
O I	17.7	15.5	O I λ 1302 is saturated
Al II	14.9	13.3	Al II λ 1670 is saturated
Si II	15.9	14.5	Five saturated lines available
Si III	15.6	13.8	Si III λ 1206 is saturated

Notes.

^a We impose the prior 10 km s⁻¹ ≤ b ≤ 20 km s⁻¹ in the Voigt profile fitting of neutral, singly, and doubly ionized species based on the COG analysis.

^b We report the best-fit column density corresponding to $b = 10$ and 20 km s⁻¹ for ions with only saturated and/or low-S/N transitions available; the b values are chosen based on the COG analysis.

corrected metallicity of $[X/H] = -0.8 \pm 0.1$ using the depletion patterns of De Cia et al. (2016). This is consistent with being drawn from the metallicity distribution of known DLAs at low redshift (Lehner et al. 2019).

3.2. An Isolated Dwarf Galaxy Pair as DLA Host

We observe two dwarf galaxies at the redshift of the DLA and employ a deep galaxy redshift survey to characterize their environment. Chen et al. (2020) described the redshift survey conducted in all CUBS fields with LDSS-3C and IMACS on Magellan and VLT-MUSE. The spectroscopic component of this survey targets galaxies fainter than 18th magnitude within $\theta \lesssim 10'$, so we primarily use photometric redshifts from the Dark Energy Survey (DES; Abbott et al. 2018). At the redshift of the DLA, a blue galaxy with $L = 0.01L_*$ has an apparent r -band magnitude of $m_r = 19.2$ assuming $M_{r,*} = -21.1$ (Cool et al. 2012), where $M_{r,*}$ is the characteristic rest-frame absolute r -band magnitude at the break of the luminosity function. We estimate the uncertainty on these photometric redshifts using 16 galaxies with $m_r < 19$ with robust spectroscopic redshifts within $\theta = 11'$. For galaxies at $z < 0.3$, we find $dz/(1+z) < 0.02$. We do not find any galaxies with $|z_{\text{phot}} - z_{\text{DLA}}| < 0.02$. There are two galaxies with $|z_{\text{phot}} - z_{\text{DLA}}| = 0.02-0.04$. The first is at $z_{\text{phot}} = 0.055$ and $d = 95$ kpc; this system has $m_r = 18.4$. The second is at $z_{\text{phot}} = 0.064$ and $d = 255$ kpc and has $m_r = 17.4$. Thus, aside from the two dwarf galaxies, there are no galaxies more luminous than $\approx 0.05L_*$ within $d \approx 350$ kpc.

As shown in Figure 2 and Table 2, the two dwarf galaxies are separated by 33 kpc and within a projected velocity of $\Delta v_g \lesssim 10$ km s⁻¹ of the DLA. We refer to these galaxies as G1 and G2, where G1 is the galaxy at a smaller impact parameter, d , with respect to the QSO. At $d = 6.2$ kpc, G1 is projected in close enough proximity to the QSO that the 3σ optical continuum light overlaps with the wing of the QSO point-spread function (PSF) on the southwest side of the galaxy. Galaxy G2 is found at the edge of the MUSE footprint at $d = 32.5$ kpc, and $\approx 15\%$ of the area within the 3σ r -band contour is found outside of the IFU coverage.

We estimate the stellar mass of both galaxies to be $\log(M_{\text{star}}/M_\odot) = 8.5 \pm 0.2$ from extinction-corrected, r -band photometry from DES using the $M_r - M_{\text{star}}$ relation derived from NASA Sloan Atlas galaxies by Liang & Chen (2014). We find comparable mass estimates from stellar population synthesis models using bagpipes. We estimate the halo mass of the galaxies to be $\log(M_h/M_\odot) = 10.8 \pm 0.2$ from the stellar mass–halo mass relation for field dwarfs determined by Read et al. (2017); this is consistent with the models of Behroozi et al. (2019). Following Maller & Bullock (2004), this yields a virial radius of $R_{\text{vir}} \approx 100_{-10}^{+20}$ kpc. Here R_{vir} is defined based on the overdensity condition of Bryan & Norman (1998) at the redshift of the dwarfs. The projected separation of the dwarfs is thus approximately one-third of their virial radii. As shown in Figure 2, the optical continuum morphology of the faint outskirts of both dwarfs shows disturbances; these irregularities are most prominent on the sides of the galaxies closest to their companion, including a faint stellar stream protruding from G1 that points toward the QSO. The

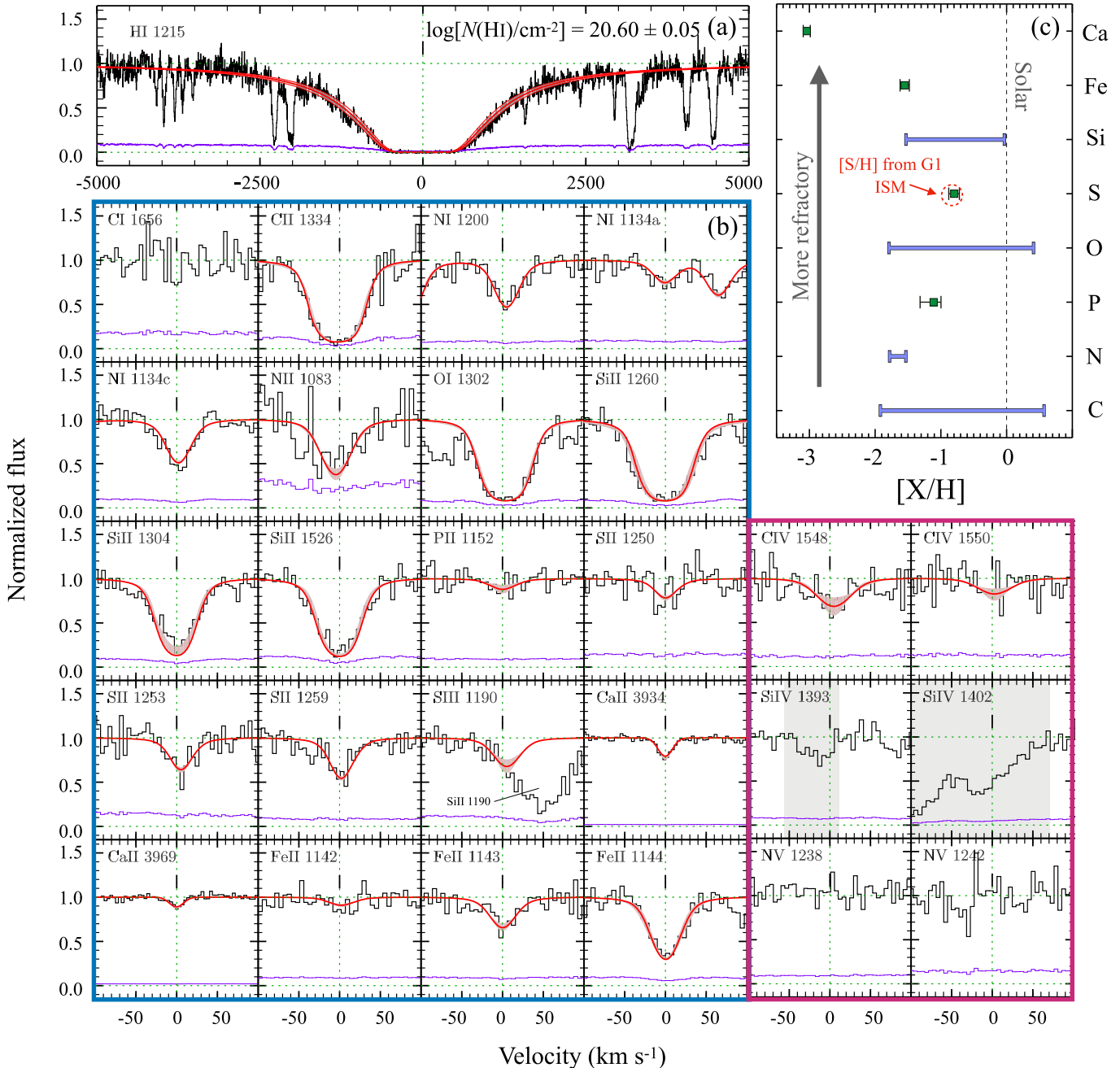


Figure 1. Shown is HST-COS and Magellan-MIKE absorption-line spectroscopy of the $z = 0.026$ DLA toward J2339–5523. (a) and (b) The data, error, and best-fit models are shown in black, purple, and red, respectively, for Ly α and a representative sample of low (left, blue box) and intermediate (right, pink box) ions. The gray shaded regions around the best-fit models represent the 1σ uncertainty. For ions without independent constraints on b , the red line is the model with $b = 15 \text{ km s}^{-1}$, and the shaded region shows the range of models with $10 \text{ km s}^{-1} \leq b \leq 20 \text{ km s}^{-1}$. The COS data are binned by two spectral pixels, or $\Delta v \approx 5 \text{ km s}^{-1}$, and the velocity zero-point is the DLA velocity. (c) Chemical abundance, $[X/H]$, derived for a range of elements ordered from most volatile (bottom) to most refractory (top). Elements with well-constrained abundances are indicated in green. The metallicity of the gas is determined to be $Z \approx 0.1Z_{\odot}$ by $[S/H]$. The decline toward lower $[X/H]$ for the most refractory elements suggests the presence of dust. The red dashed circle shows the 1σ range of $[S/H]$ measured for the brightest star-forming region in the more proximate dwarf, demonstrating strong consistency in the α -element abundances of the damped absorber and the ISM of the host galaxy.

extinction-corrected H α luminosity of G1, $L(\text{H}\alpha) \approx 8 \times 10^{39} \text{ erg s}^{-1}$, suggests a star formation rate (SFR) of $\approx 0.04 M_{\odot} \text{ yr}^{-1}$ following the relation of Calzetti (2008). About two-thirds of the star formation is found in the bright, star-forming knot labeled G1R1 in Figure 2. Galaxy G2 is $\approx 40\%$ dimmer than G1 in H α and thus has $\text{SFR}(\text{H}\alpha) \approx 0.03 M_{\odot} \text{ yr}^{-1}$ (a small fraction of the H α flux may be unaccounted for due to the proximity of the galaxy to the edge of the detector).

3.3. Neutral Gas Properties of DLA Host

We detect spatially extended H I 21 cm emission that reveals a neutral gas envelope surrounding G1 and G2 on a scale of $>40 \text{ kpc}$, including an apparent tidal bridge between them. We display the H I column density contours in Figure 2. The bridge has a width of $\sim 20''$, or 10 kpc, at the level of $5 \times 10^{19} \text{ cm}^{-2}$ and is thus resolved by MeerKAT’s synthesized beam (FWHM = 4 kpc \times 3 kpc). The total integrated line flux of

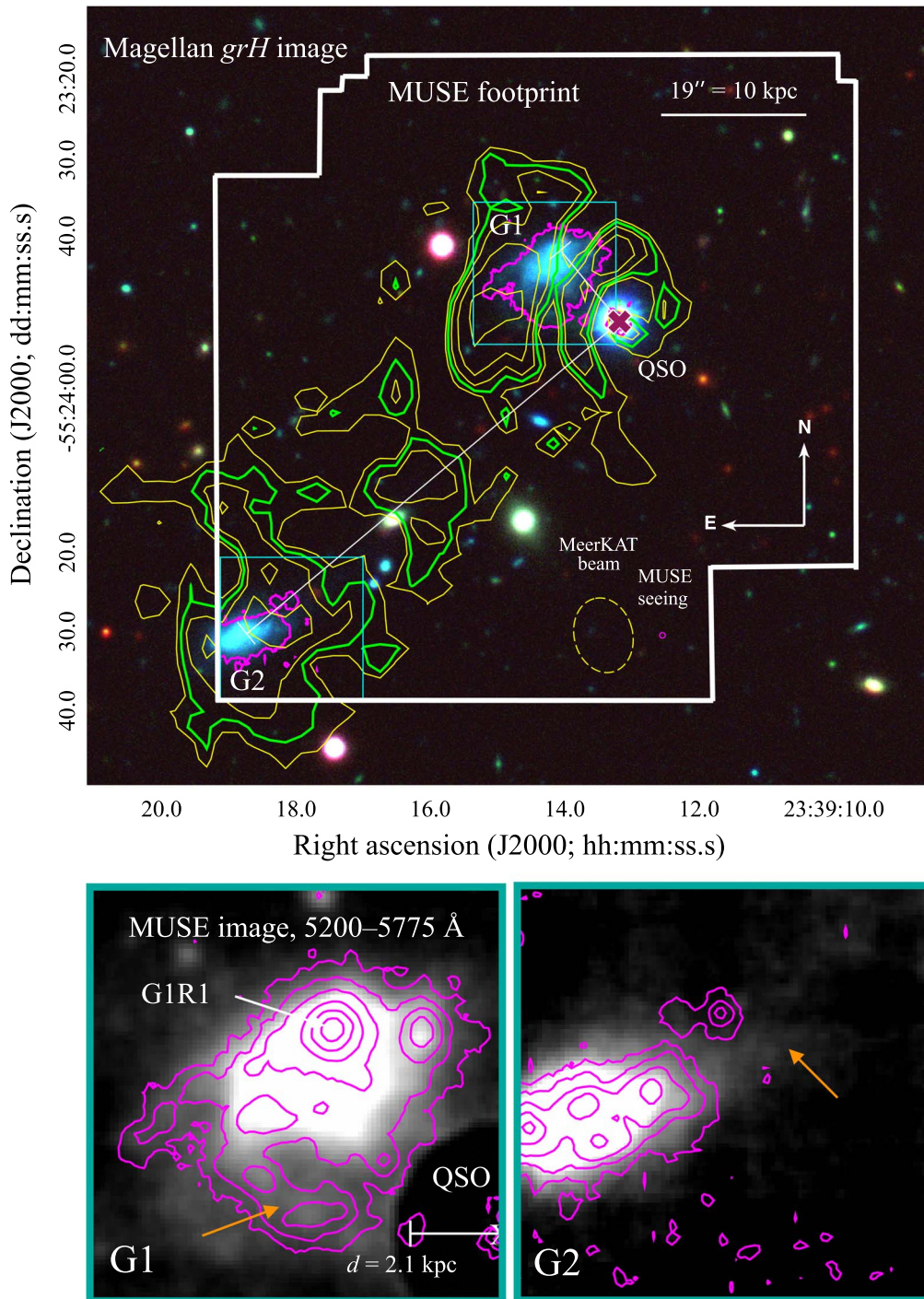


Figure 2. Multiwavelength view of the DLA host. In the top panel, a Magellan *grH* image shows two blue dwarf galaxies at the redshift of the DLA at impact parameters of $d = 6.2$ (G1) and 32.5 (G2) kpc. We overlay H I column density contours of $5 \times 10^{19} \times (1, 8, 16, 32) \text{ cm}^{-2}$ from the MeerKAT observations in yellow, and we indicate the DLA column density threshold, $2 \times 10^{20} \text{ cm}^{-2}$, in green. The average 3σ column density sensitivity across the map is $3.2 \times 10^{20} \text{ cm}^{-2}$ (e.g., de Blok et al. 2018). The MeerKAT beam is shown in yellow at the lower right. We also overlay the 3σ H α contours from MUSE (magenta), which correspond to a surface brightness of 2.6×10^{-18} and $3.8 \times 10^{-18} \text{ erg s}^{-1} \text{ cm}^{-2} \text{ arcsec}^{-2}$ for G1 and G2, respectively. In the bottom panels, we show additional H α contours at the 3σ , 10σ , 30σ , 100σ , 300σ , and 1000σ levels on a white-light image constructed from the MUSE cube between 5200 and 5775 \AA (chosen to avoid emission lines). The H α emission is not detected at the QSO location; the contour shown at the QSO position is a result of residuals from the QSO PSF subtraction. However, an H α blob is detected at an impact parameter of $d = 2.1$ kpc. We label the brightest star-forming region in G1 as G1R1. The stellar continuum shows evidence of disturbance at its faint outskirts, including possible stellar streams pointing toward the QSO, as indicated by orange arrows. The H α features at the bottom of the G2 frame are due to elevated noise at the edge of the MUSE detector.

the system is $0.44 \pm 0.06 \text{ Jy km s}^{-1}$, which corresponds to a total HI gas mass of $M(\text{HI}) \approx 1.3 \times 10^9 M_{\odot}$. If we bisect the gas distribution at the midpoint between the galaxies, the two dwarfs are associated with nearly the same HI mass.

As shown in Figure 2, the QSO sight line intersects the outer gaseous envelope of G1. In the vicinity of the QSO, HI emission from several voxels in the image cube contributes to the HI 21 cm column density. The emission is detected in

Table 2
Properties of the Dwarf Galaxy Hosts of the $z = 0.026$ DLA

	G1	G2
Name	CUBS2339z002_G6	CUBS2339z002_G32
R.A.	23h39m14.11s	23h39m18.82s
decl.	-55d23m41.9s	-55d24m30.5s
$\Delta\alpha$ (arcsec) ^a	+7.6	+47.7
$\Delta\delta$ (arcsec) ^a	+9.0	-39.7
θ (arcsec) ^a	11.8	62.0
d (kpc) ^a	6.2	32.5
z ^b	0.02608	0.02604
Δv_z (km s ⁻¹) ^c	11.2 ± 0.1	0.4 ± 0.1
m_r (mag) ^d	18.3 ± 0.3	18.3 ± 0.3
M_r (mag)	-17.0 ± 0.3	-17.0 ± 0.3
$\log(M_{\text{star}}/M_{\odot})$ ^e	8.5 ± 0.2	8.5 ± 0.2
SFR(H α) (M_{\odot} yr ⁻¹)	≈0.04	≈0.03
$M(\text{H I})$ (M_{\odot})	≈7 × 10 ⁸	≈7 × 10 ⁸
$M(\text{H II})$ (M_{\odot})	~10 ⁷ -10 ⁸	~10 ⁷ -10 ⁸

Notes.

^a R.A. offsets ($\Delta\alpha$), decl. offsets ($\Delta\delta$), angular separations (θ), and impact parameters (d) are measured with respect to the QSO position at R.A., decl. = 23h39m13.22s, -55d23m50.8s.

^b Light-weighted mean redshift.

^c Velocity offset with respect to $z_{\text{DLA}} = 0.02604$.

^d The r -band apparent magnitudes are from DES (Abbott et al. 2018) and corrected for internal extinction adopting a characteristic $E(B - V) = 0.05$ and 0.1 for G1 and G2, respectively (see Section 3.4.3).

^e Determined using the $M_r - M_{\text{star}}$ relation of Liang & Chen (2014) and stellar population modeling from `bagpipes` (Carnall et al. 2018).

individual spectral channels at the 2σ - 3σ level. Within the MeerKAT synthesized beam, the characteristic column density at the location of the peak flux density of the QSO is $\log[N(\text{H I})/\text{cm}^{-2}] \approx 20.6$. Despite the possible impact of beam dilution in a clumpy medium, this is remarkably consistent with the column density determined from the HST-COS absorption-line spectroscopy.

The QSO J2339-5523 is unresolved (size < 300 pc) in the MeerKAT image. We visually examined the spectral line image cube and confirmed that no negative features representing H I 21 cm absorption at the $> 2\sigma$ level ($\int \tau dv = 0.028 \text{ km s}^{-1}$) are present toward the QSO. The strength of the H I 21 cm absorption depends on the H I column density, as well as the spin temperature, T_s , and the covering factor of the absorbing gas, f_c . If the radio-emitting region of the QSO is more spatially extended than the absorbing gas, then $f_c < 1$. The H I column density toward the UV-emitting region of the QSO is well constrained through the HST-COS observations of the DLA. If the UV- and radio-emitting regions of the QSO are spatially aligned, we can use the measured $N(\text{H I})$ from COS to constrain the ratio of the spin temperature to the covering factor. Using a 5σ upper limit on H I 21 cm absorption in the unsmoothed MeerKAT spectrum with a spectral rms of $0.44 \text{ mJy beam}^{-1} \text{ channel}^{-1}$, we estimate a lower limit of $T_s/f_c > 1880 \text{ K}$ assuming an FWHM of 17 km s^{-1} ($b = 10 \text{ km s}^{-1}$) for the H I absorption line based on the metal lines detected in the COS and MIKE spectra.

In the top panels of Figure 3, we show the line-of-sight velocity and velocity dispersion of the neutral gas traced by H I 21 cm emission. The velocity shear across the neutral gas distribution is $\approx \pm 20 \text{ km s}^{-1}$. The characteristic velocity dispersion within the bodies of G1 and G2 is 10 - 15 km s^{-1} , and this value is a factor of 2 higher in parts of the extended

medium, suggesting possible dynamical disturbance. Due to the relatively small number of MeerKAT beams sampling the gas distribution, we cannot draw strong conclusions about whether the bridge gas arises from G1 or G2. It is also not clear if the gas distribution in either galaxy is disklike; there is no definitive evidence for organized rotation, and it is common for the gas content in galaxies of this mass to have significant dispersion support (e.g., El-Badry et al. 2018).

3.4. Warm Ionized Gas Properties of DLA Host

We analyze the warm ionized medium (WIM) in both dwarf galaxies with the goal of comparing the observable properties of the interstellar medium (ISM) with those of the damped absorber to better characterize the origin of the neutral gas envelope. Among the emission lines covered by MUSE are H α , H β , [O III] $\lambda\lambda 4960, 5008$, [N II] $\lambda\lambda 6549, 6585$, [S II] $\lambda\lambda 6718, 6732$, and [S III] $\lambda 6313, 9071$, all of which are detected in at least one star-forming region in one or both galaxies.

3.4.1. WIM Mass and Morphology

As shown in Figure 2, there is no evidence of spatially extended optical line emission on scales larger than the stellar components of G1 and G2. The 3σ H α surface brightness detection threshold in the vicinity of G1 (G2) is $2.6 \times 10^{-18} \text{ erg s}^{-1} \text{ cm}^{-2} \text{ arcsec}^{-2}$ ($3.8 \times 10^{-18} \text{ erg s}^{-1} \text{ cm}^{-2} \text{ arcsec}^{-2}$). Notably, the WIM does not overlap with the quasar sight line at the detection threshold of the data. The line-emitting feature in closest projected proximity to the quasar sight line ($d \approx 2 \text{ kpc}$) is an isolated cloud separated from the main body of G1 in the 3σ H α surface brightness contour (see Figure 2). We used an optimal extraction method implemented in `CubExtractor` to search for H α and [N II] emission on top of the QSO, but the noise properties of the region affected by the bright QSO PSF prohibit a sensitive constraint on the H α surface brightness at this location.

We estimate the warm ionized gas mass in the ISM of G1 and G2 as follows. For a clumping factor $\mathcal{C} \equiv \langle n_e^2 \rangle / \langle n_e \rangle^2$, the H α surface brightness depends on the mean electron density, $\langle n_e \rangle$, and the path length through the gas, L , according to

$$I(\text{H}\alpha) \approx 2 \times 10^{-15} \frac{\mathcal{C} \langle n_e \rangle^2}{(1+z)^4} \frac{L}{\text{kpc}} \text{ erg s}^{-1} \text{ cm}^{-2} \text{ arcsec}^{-2}. \quad (1)$$

Here the electron density is in units of cm^{-3} , and we assume an electron temperature $T_e = 10^4 \text{ K}$. If the ionized gas is found in a relatively thin disk ($L \approx 1 \text{ kpc}$) in G1, then $M(\text{H II}) \approx 4$ - $10 \times 10^7 M_{\odot}$ for \mathcal{C} between 10 and 1. If, instead, L is closer to the projected size of the line-emitting region ($L \approx 7 \text{ kpc}$), then the ionized gas mass may be as high as 0.9 - $3 \times 10^8 M_{\odot}$ for the same range of clumping factors. At approximately half of the H α luminosity, the ionized gas mass estimates for G2 are roughly half of those for G1. Across these models, the electron density varies between $\langle n_e \rangle \approx 0.005$ and 1 cm^{-3} , which is consistent with the constraint from $I([\text{S II}] \lambda 6718)/I([\text{S II}] \lambda 6732)$ that $n_e \lesssim 10^2 \text{ cm}^{-3}$ (e.g., Osterbrock & Ferland 2006). Thus, the warm ionized phase of the ISM likely contributes between a few percent and 50% as much mass as the neutral phase.

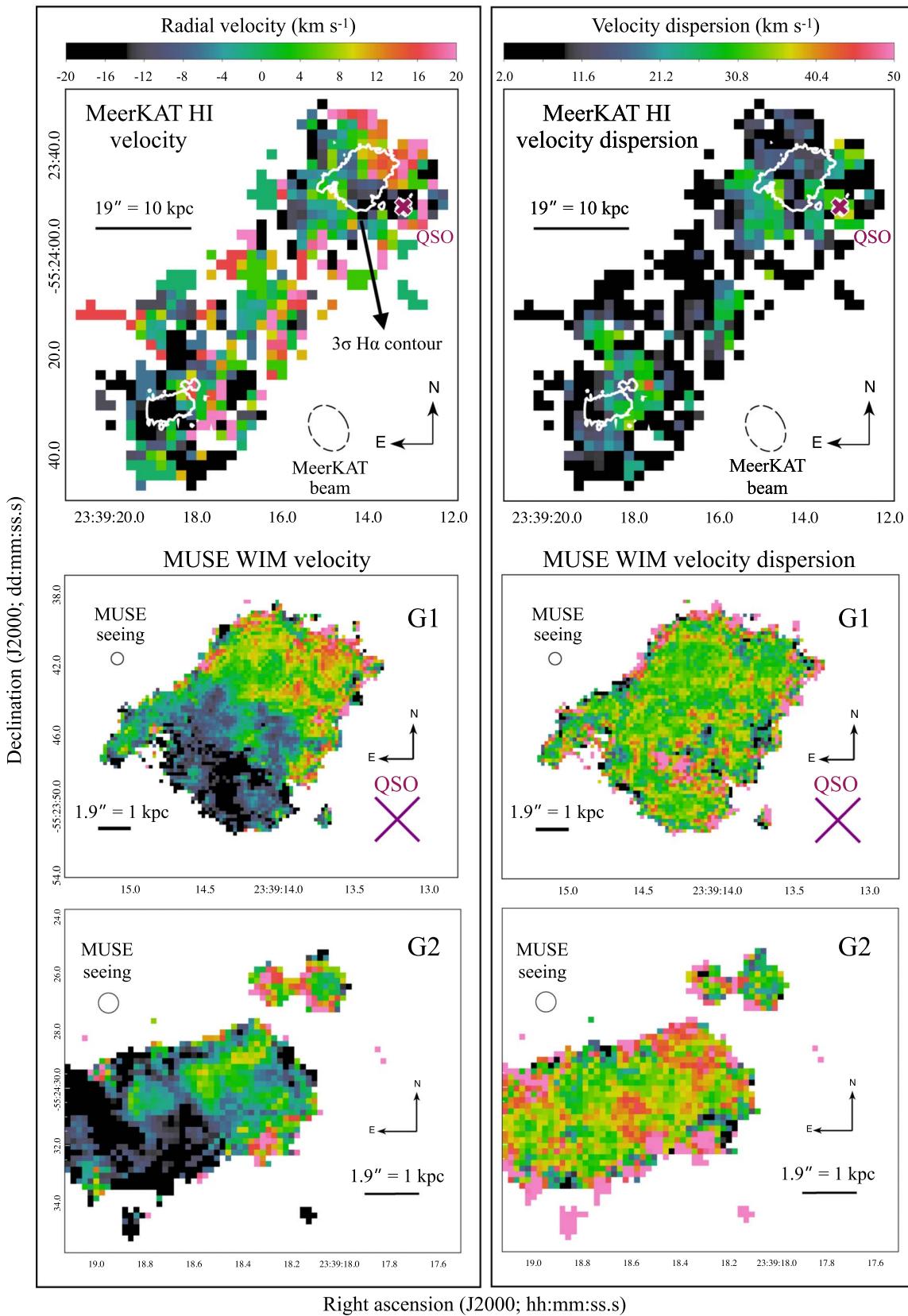


Figure 3. In the left panels, the radial velocities of the neutral gas traced by H I 21 cm emission (top) and ionized gas observed via optical line emission (bottom) show notable consistency with the velocity of the DLA, where the velocity zero-point is set by the DLA redshift ($z = 0.026$). In the right panels, we show the velocity dispersion of the multiphase gas. In the bodies of the dwarf galaxies, the characteristic dispersion is 10–15 km s⁻¹ in the neutral gas and 30 km s⁻¹ in the ionized gas. While this hints at modest turbulence in the latter phase, the optical emission lines are largely unresolved (the MUSE spectral resolution at H α has an FWHM of ≈ 113 km s⁻¹, or $\sigma \approx 48$ km s⁻¹). The isolated clumps on the southern side of G2 are marginal detections with uncertain line widths.

3.4.2. WIM Kinematics

We show the generally quiescent kinematics of the warm ionized gas in the dwarf galaxies in Figure 3. In G1, the line-of-sight velocities generally fall in the range $-25 \text{ km s}^{-1} \leq v_{\text{rad}} \leq +25 \text{ km s}^{-1}$; an ordered pattern is evident, with the southern side of the galaxy approaching and the northern side receding. The discrete cloud closest in projection to the QSO has a median $v_{\text{rad}} = -4 \pm 10 \text{ km s}^{-1}$, and comparable velocity offsets with respect to the absorber are seen in the portion of the main body of the galaxy in closest projected proximity. We find similar results for G2, with milder evidence for an ordered velocity gradient of a few tens of kilometers per second from the southeast (approaching) to northwest (receding) side. The characteristic velocity dispersion of the WIM in both galaxies is $\sigma \equiv \text{FWHM}/(2\sqrt{2}\ln(2)) = 30\text{--}40 \text{ km s}^{-1}$ (corrected for spectral resolution), which is not resolved at the spectral resolution of the MUSE instrument. There is a marked consistency between the velocity centroids of the DLA and the H I and H II gas.

3.4.3. WIM Metallicity and Dust Content

For G1R1, we detect both the auroral [S III] $\lambda 6313$ and the nebular [S III] $\lambda 9071$ transitions, permitting a measurement of T_e and thus our most direct constraint on the gas-phase metallicity. In the top left panel of Figure 4, we show the aperture within which both lines are detected at the 3σ level, and we find $I([\text{S III}] \lambda 9533 + \lambda 9071)/I([\text{S III}] \lambda 6313) = 29.0 \pm 0.9$ within this region (note that the nebular lines have a fixed ratio of $I([\text{S III}] \lambda 9533)/I([\text{S III}] \lambda 9071) = 2.44$). Following Osterbrock & Ferland (2006), this yields $T_e \approx 1.4 \times 10^4 \text{ K}$ at the density constrained by the [S II] doublet ($n_e \lesssim 10^2 \text{ cm}^{-3}$). Adopting this value of T_e , we use the $I([\text{S II}] \lambda 6718)/I(\text{H}\alpha)$ and $I([\text{S III}] \lambda 9533)/I(\text{H}\alpha)$ line ratios to estimate $\text{S}/\text{H} = \text{S}^+/\text{H} + \text{S}^{++}/\text{H} \approx 10\%\text{--}20\%$ of the solar value, consistent with the abundance determined for the DLA in Section 3.1.

We additionally detect several strong-line metallicity indicators in multiple star-forming regions in both galaxies, including $\text{N}_2 = I([\text{N II}] \lambda 6585)/I(\text{H}\alpha)$ (e.g., Pettini & Pagel 2004, hereafter PP04; see Figure 4). Following PP04, we find $12 + \log(\text{O}/\text{H}) \approx 8.0$ (20% solar) from N_2 in G1R1 (note the 0.2 dex systematic uncertainty in the PP04 relation). We observe values up to $12 + \log(\text{O}/\text{H}) = 8.3\text{--}8.4$ (40%–50% solar) in lower surface brightness regions of this galaxy, but we regard this as an upper limit due to the likely presence of diffuse ionized gas that elevates the observed line ratios and thus biases the metallicity measurement (e.g., Zhang et al. 2017; Vale Asari et al. 2019). In the star-forming regions of G2, $12 + \log(\text{O}/\text{H})$ is generally ≈ 0.1 dex higher than in G1, suggesting slightly elevated metallicity in this galaxy. We corroborate a metallicity of a few tens of percent solar for G1 and G2 using Cloudy photoionization models to reproduce the observable emission-line ratios (Ferland et al. 2017). The dust extinction maps shown in the bottom panel of Figure 4 indicate a characteristic $E(B - V) = 0.05$ and 0.1 for G1 and G2, respectively. This is comparable to the characteristic $E(B - V) \approx 0.1$ found for galaxies of this mass by Salim et al. (2018), suggesting that G1 and G2 are typical in their dust content.

4. Discussion and Concluding Remarks

This case study clearly confirms an association between the $z = 0.026$ DLA and a neutral gas envelope surrounding two interacting dwarf galaxies in a rare instance of spatially resolved H I 21 cm emission that is coincident with a UV-selected DLA outside of the optical extent of a galaxy.²⁵ Both the ISM of G1 and the DLA have relatively low metallicities ($Z \approx 0.1Z_{\odot}$), contain dust, and show comparable kinematics, suggesting that the gas in the envelope originated in the ISM of the dwarf galaxies. Opportunities to compare the chemical enrichment of DLAs with that of the ionized ISM of the host galaxies remain rare. Aloisi et al. (2003) used a down-the-barrel approach to demonstrate that the neutral ISM has α -element abundances below those of the H II regions in I Zw 18, implying that the star-forming regions are enriched by recent star formation. In contrast, the DLA galaxy SBS 1543+593 has consistent α -element abundances in its H II regions and the damped absorber that coincides with its inner ISM (Schulte-Ladbeck et al. 2004, 2005; Bowen et al. 2005). The J2339–5523 DLA provides a second case of consistency between the α -element abundances of the damped absorber and the H II regions in the host galaxy. Establishing a statistical sample of such systems in the local universe will shed light on the nature of the host galaxies of low-metallicity DLAs at higher redshift.

Correlations between galaxy mass and/or morphology, optical size, and H I size are well characterized and establish expectations for the extent of the neutral gas distributions around the dwarf galaxies. Cayatte et al. (1994) reported mean H I-to-optical diameter ratios in the range 1.5–1.9 for disk galaxies with a variety of morphological types in the field, while Broeils & Rhee (1997) found a consistent mean value of 1.7 ± 0.5 independent of morphological type. The equivalent ratio for G1 and G2 is between 2 and 3 and thus falls $1\sigma\text{--}2\sigma$ toward the upper end of the distribution. Additionally, the LITTLE THINGS H I 21 cm survey of nearby dwarf irregular galaxies (Hunter et al. 2012), as well as dwarf galaxy samples from Kovač et al. (2009) and Lelli et al. (2014), suggests a relatively flat distribution of H I-to-optical diameter ratios, with some systems in the range of 2–4 (Bosma 2017).

Wang et al. (2016) used a large sample of more than 500 galaxies from various samples to demonstrate a tight relation between H I diameter, $D(\text{H I})$, and $M(\text{H I})$. The relation suggests an overall similarity in the evolution of gas-rich galaxies, from small dwarfs to large spirals. The observed neutral gas mass is $M(\text{H I}) \approx 7 \times 10^8 M_{\odot}$ for both dwarfs if we bisect the total H I distribution at their midpoint. This corresponds to a size of $D(\text{H I}) \approx 16 \text{ kpc}$ based on the Wang et al. (2016) relation. For G1, the extent of the H I is 14 kpc at a gas surface density of $\Sigma(\text{H I}) = 1 M_{\odot} \text{ pc}^{-2}$, well within the 3σ scatter of the relation. In summary, excluding the bridge, the spatial extent of the observed H I distribution around G1 and G2 is consistent with the known H I size–mass relation. This is in line with the demonstrated robustness of this relation in the presence of environmental processes that cause a truncation of the H I distribution but leave the H I size–mass relation unaffected (Stevens et al. 2019).

Following King (1962), we characterize the impact of tidal interaction on the dwarf galaxies. For a body, M_1 , on a circular

²⁵ See Chengalur & Kanekar (2002) for the one known instance inside of the optical extent.

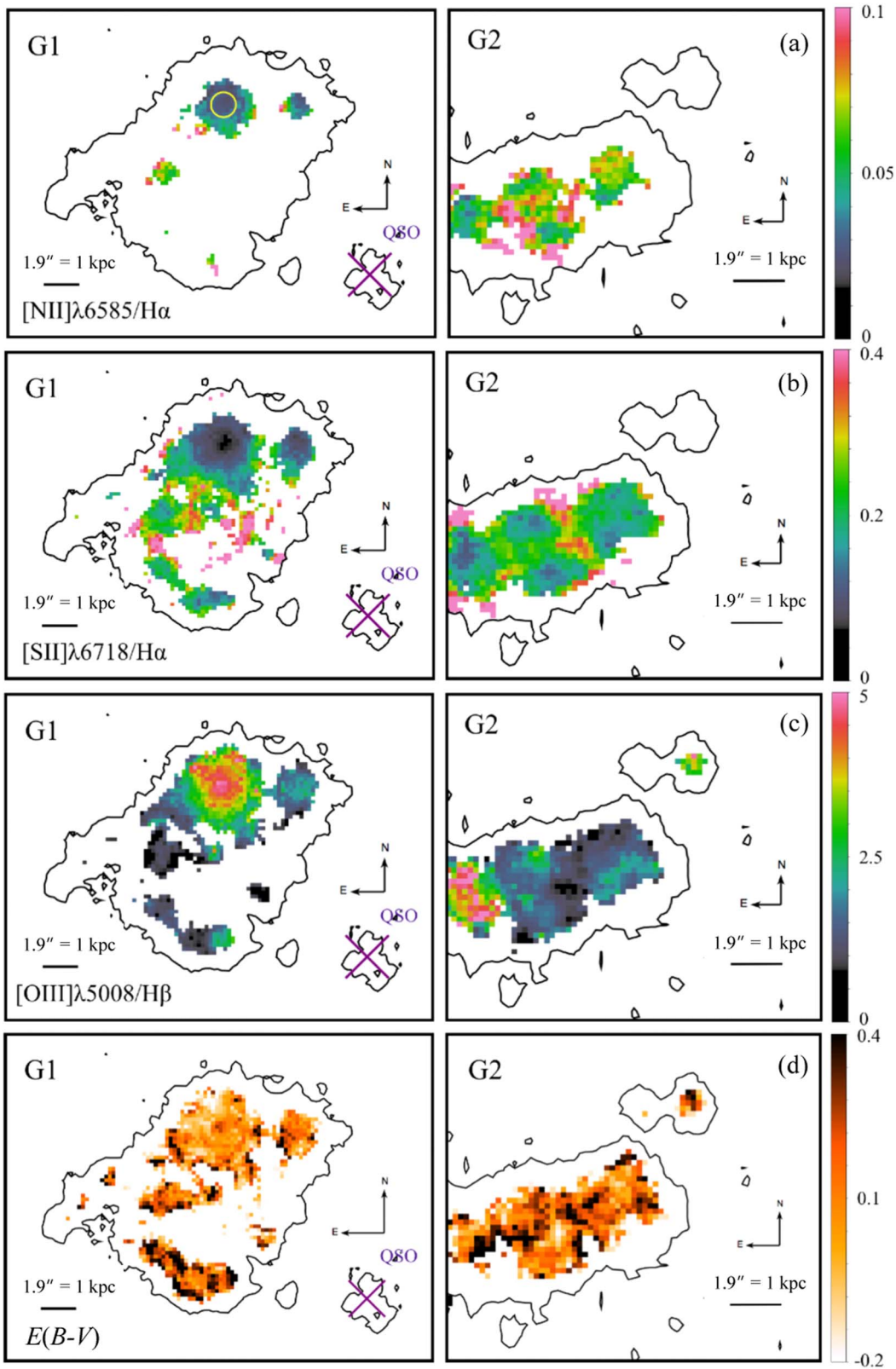


Figure 4. Maps of G1 (left) and G2 (right), showing the emission-line intensity ratios (a) $I([\text{N II}] \lambda 6585)/I(\text{H}\alpha)$, (b) $I([\text{S II}] \lambda 6718)/I(\text{H}\alpha)$, and (c) $I([\text{O III}] \lambda 5008)/I(\text{H}\beta)$. In panel (d), we show the reddening, $E(B - V)$, as determined from the Balmer decrement, indicating the presence of dust in the ISM. The included spaxels have detections of both relevant lines at the $\geq 3\sigma$ level. The black contour is the 3σ $\text{H}\alpha$ detection threshold. The contour shown at the QSO location is a result of residuals from the QSO PSF subtraction. In the left panels, the stellar stream pointing toward the QSO from G1 is seen to be accompanied by warm ionized gas that contains dust. The aperture indicated in yellow at the top left is the region where we detect both the auroral $[\text{S III}] \lambda 6313$ and the nebular $[\text{S III}] \lambda 9071$ lines that permit a direct measurement of T_e and thus $[\text{S}/\text{H}]$.

orbit in the gravitational field of M_2 , the radius beyond which tidal stripping will occur, r_t , can be expressed as

$$r_t = r_{\text{sep}} \left(\frac{M_1}{3M_{2,\text{encl}}} \right)^{1/3}. \quad (2)$$

Here r_{sep} is the distance between the objects at closest approach, and $M_{2,\text{encl}}$ is the mass of M_2 enclosed within r_{sep} . We assume that the current projected separation of the dwarf galaxies is their distance of closest approach ($r_{\text{sep}} = 33$ kpc) and calculate $M_{2,\text{encl}}$ including contributions from stars, gas, and a dark matter halo described by a Navarro–Frenk–White profile (Navarro et al. 1997) with a concentration parameter of $c = 10\text{--}20$ (e.g., Zhao et al. 2009). Taking M_1 to be the stellar, gas, and dark matter mass contained within the stellar body, we find that the truncation radius is in the range $r_t \approx 11\text{--}13$ kpc. This exceeds the observed value of ≈ 7 kpc, which suggests either that the galaxies are intrinsically small enough to avoid tidal truncation or that a closer approach between the dwarf galaxies in the past is responsible for truncating them to their current size. The latter scenario is supported by the presence of the H I bridge and the faint irregularities observed in the outskirts of the stellar and ionized gas distributions of both galaxies. The observed offset in the centers of the stellar and neutral gas distributions in G1 may also indicate tidal disruption of the gaseous component of the dwarf. All evidence considered, it is likely that the DLA arises from gas that originated in the ISM of G1 and has since been perturbed by tidal interaction.

The definitive lack of a massive companion allows us to isolate the effects of dwarf–dwarf interactions on their gaseous reservoirs in the absence of processes such as ram pressure stripping in a massive, hot halo. In this system, the cross section for producing damped absorbers is much larger than the inner ISM alone. Gas with $N(\text{H I}) \geq 2 \times 10^{20} \text{ cm}^{-2}$ is seen in the ISM, the outskirts of the H I distributions, and the adjoining bridge, informing the diversity of environments that can host DLAs. It is likely that the cross section for ionized absorbers is larger still but below the MUSE detection threshold; the $z = 0.364$ Lyman limit system (LLS) detected in CUBS toward J0248–4048 arises from an analogous system of a relatively isolated dwarf galaxy pair at an impact parameter of several tens of kiloparsecs. The metallicity and chemical abundance pattern of the LLS suggests that it arises in tidal feature(s) composed of former ISM material (Zahedy et al. 2021). The Magellanic Stream appears to be a local example of a multiphase feature whose formation was dominated by tidal forces from the Large Magellanic Cloud acting on its smaller companion on initial infall into the halo of the Milky Way (e.g., Besla et al. 2012). Thus, models of the evolution of dwarf galaxy pairs—both within and outside of the halos of massive galaxies—must account for the role of dwarf–dwarf interactions in producing tidal features that enhance the cross section for neutral absorbers.

Our comprehensive characterization of the galactic origin of the $z = 0.026$ DLA was only made possible by the joint analysis of HST UV absorption-line and MeerKAT H I 21 cm emission-line data alongside detailed galaxy spectroscopy. As we move further into the era of the Square Kilometre Array and the next-generation Very Large Array with much higher sensitivity and spatial resolution, leveraging the time-limited

availability of space-based UV resources in conjunction with spatially resolved 21 cm mapping will be critical to enhance our understanding of the diverse galactic environments that host the majority of the neutral gas in the universe.

We thank Tom Cooper for useful discussions and his valuable contributions to the CUBS galaxy redshift survey, Zhijie Qu for helpful comments on the paper draft, and Alex Drlica-Wagner for assistance in extracting photometric data from the Dark Energy Survey catalog. We thank the anonymous referee for constructive comments that improved the presentation of the paper.

E.B. and H.W.C. acknowledge partial support from grants HST-GO-15163.001A and NSF AST-1715692. S.C. gratefully acknowledges support from the European Research Council (ERC) under the European Union’s Horizon 2020 research and innovation program grant agreement No. 864361. K.L.C. acknowledges partial support from NSF AST-1615296. C.A.F.G. was supported by NSF through grants AST-1715216 and AST-2108230 and CAREER award AST-1652522; NASA through grant 17-ATP17-0067; STScI through grant HST-AR-16124.001-A; and the Research Corporation for Science Advancement through a Cottrell Scholar Award. J.K.K. acknowledges support by the Swiss National Science Foundation under grant 185692. S.L. was funded by FONDECYT grant No. 1191232. F.S.Z. is grateful for the support of a Carnegie Fellowship from the Observatories of the Carnegie Institution for Science. This material is based upon work supported by NASA under award No. 80GSFC21M0002.

This work is based on observations made with ESO telescopes at the Paranal Observatory under program ID 0104.A-0147(A), observations made with the 6.5 m Magellan Telescopes located at Las Campanas Observatory, and spectroscopic data gathered under the HST-GO-15163.01A program using the NASA/ESA Hubble Space Telescope, operated by the Space Telescope Science Institute and the Association of Universities for Research in Astronomy, Inc., under NASA contract NAS 5-26555. The MeerKAT telescope is operated by the South African Radio Astronomy Observatory, which is a facility of the National Research Foundation, an agency of the Department of Science and Innovation. The MeerKAT data were processed using the MALS computing facility at IUCAA (<https://mals.iucaa.in/releases>).

This project used public archival data from the Dark Energy Survey (DES). Funding for the DES Projects has been provided by the U.S. Department of Energy, the U.S. National Science Foundation, the Ministry of Science and Education of Spain, the Science and Technology Facilities Council of the United Kingdom, the Higher Education Funding Council for England, the National Center for Supercomputing Applications at the University of Illinois at Urbana-Champaign, the Kavli Institute of Cosmological Physics at the University of Chicago, the Center for Cosmology and Astro-Particle Physics at the Ohio State University, the Mitchell Institute for Fundamental Physics and Astronomy at Texas A&M University, Financiadora de Estudos e Projetos, Fundação Carlos Chagas Filho de Amparo à Pesquisa do Estado do Rio de Janeiro, Conselho Nacional de Desenvolvimento Científico e Tecnológico and the Ministério da Ciência, Tecnologia e Inovação, the Deutsche Forschungsgemeinschaft, and the Collaborating Institutions in the Dark Energy Survey.

The Collaborating Institutions are Argonne National Laboratory, the University of California at Santa Cruz, the University of Cambridge, Centro de Investigaciones Energéticas,

Medioambientales y Tecnológicas-Madrid, the University of Chicago, University College London, the DES-Brazil Consortium, the University of Edinburgh, the Eidgenössische Technische Hochschule (ETH) Zürich, Fermi National Accelerator Laboratory, the University of Illinois at Urbana-Champaign, the Institut de Ciències de l'Espai (IEEC/CSIC), the Institut de Física d'Altes Energies, Lawrence Berkeley National Laboratory, Ludwig-Maximilians Universität München and the associated Excellence Cluster Universe, the University of Michigan, the National Optical Astronomy Observatory, the University of Nottingham, The Ohio State University, the OzDES Membership Consortium, the University of Pennsylvania, the University of Portsmouth, SLAC National Accelerator Laboratory, Stanford University, the University of Sussex, and Texas A&M University.

Based in part on observations at Cerro Tololo Inter-American Observatory, National Optical Astronomy Observatory, which is operated by the Association of Universities for Research in Astronomy (AURA) under a cooperative agreement with the National Science Foundation. The National Radio Astronomy Observatory is a facility of the National Science Foundation operated under cooperative agreement by Associated Universities, Inc. This research has made use of NASA's Astrophysics Data System and the NASA/IPAC Extragalactic Database (NED), which is operated by the Jet Propulsion Laboratory, California Institute of Technology, under contract with the National Aeronautics and Space Administration. This work made use of the KUBEVIZ software, which is publicly available at <http://www.mpe.mpg.de/~dwilman/kubeviz/>.

Software: ARTIP (Gupta et al. 2021), bagpipes (Carnall et al. 2018), CalcOS, CarPy (Kelson 2003), CLOUDY (Ferland et al. 2013), CubExtractor (Cantalupo et al. 2019), KUBEVIZ, SOFIA (Serra et al. 2015; Westmeier et al. 2021).

ORCID iDs

Erin Boettcher  <https://orcid.org/0000-0003-3244-0409>
 Neeraj Gupta  <https://orcid.org/0000-0001-7547-4241>
 Hsiao-Wen Chen  <https://orcid.org/0000-0001-8813-4182>
 Mandy C. Chen  <https://orcid.org/0000-0002-8739-3163>
 Gyula I. G. Józsa  <https://orcid.org/0000-0003-0608-6258>
 Gwen C. Rudie  <https://orcid.org/0000-0002-8459-5413>
 Sebastiano Cantalupo  <https://orcid.org/0000-0001-5804-1428>
 Sean D. Johnson  <https://orcid.org/0000-0001-9487-8583>
 S. A. Balashev  <https://orcid.org/0000-0002-3814-9666>
 Françoise Combes  <https://orcid.org/0000-0003-2658-7893>
 Kathy L. Cooksey  <https://orcid.org/0000-0001-5810-5225>
 Claude-André Faucher-Giguère  <https://orcid.org/0000-0002-4900-6628>
 Jens-Kristian Krogager  <https://orcid.org/0000-0002-4912-9388>
 Sebastian Lopez  <https://orcid.org/0000-0003-0389-0902>
 Emmanuel Momjian  <https://orcid.org/0000-0003-3168-5922>
 Pasquier Noterdaeme  <https://orcid.org/0000-0002-5777-1629>
 Marc Rafelski  <https://orcid.org/0000-0002-9946-4731>
 Raghunathan Srianand  <https://orcid.org/0000-0002-9062-1921>
 Gregory L. Walth  <https://orcid.org/0000-0002-6313-6808>
 Fakhri S. Zahedy  <https://orcid.org/0000-0001-7869-2551>

References

Abbott, T. M. C., Abdalla, F. B., Allam, S., et al. 2018, *ApJS*, 239, 18
 Aloisi, A., Savaglio, S., Heckman, T. M., et al. 2003, *ApJ*, 595, 760
 Asplund, M., Grevesse, N., Sauval, A. J., & Scott, P. 2009, *ARA&A*, 47, 481

Battisti, A. J., Meiring, J. D., Tripp, T. M., et al. 2012, *ApJ*, 744, 93
 Behroozi, P., Wechsler, R. H., Hearin, A. P., & Conroy, C. 2019, *MNRAS*, 488, 3143
 Besla, G., Kallivayalil, N., Hernquist, L., et al. 2012, *MNRAS*, 421, 2109
 Boettcher, E., Chen, H.-W., Zahedy, F. S., et al. 2021, *ApJ*, 913, 18
 Borthakur, S., Momjian, E., Heckman, T. M., et al. 2019, *ApJ*, 871, 239
 Bosma, A. 2017, in *Outskirts of Galaxies*, ed. J. H. Knapen, J. C. Lee, & A. Gil de Paz, Vol. 434 (Berlin: Springer), 209
 Bowen, D. V., Huchtmeier, W., Brinks, E., Tripp, T. M., & Jenkins, E. B. 2001, *A&A*, 372, 820
 Bowen, D. V., Jenkins, E. B., Pettini, M., & Tripp, T. M. 2005, *ApJ*, 635, 880
 Broeils, A. H., & Rhee, M. H. 1997, *A&A*, 324, 877
 Bryan, G. L., & Norman, M. L. 1998, *ApJ*, 495, 80
 Calzetti, D. 2008, in *ASP Conf. Ser. 390, Pathways Through an Eclectic Universe*, ed. J. H. Knapen, T. J. Mahoney, & A. Vazdekis (San Francisco, CA: ASP), 121
 Calzetti, D., Kinney, A. L., & Storchi-Bergmann, T. 1994, *ApJ*, 429, 582
 Cantalupo, S., Pezzulli, G., Lilly, S. J., et al. 2019, *MNRAS*, 483, 5188
 Cardelli, J. A., Clayton, G. C., & Mathis, J. S. 1989, *ApJ*, 345, 245
 Carilli, C. L., & van Gorkom, J. H. 1992, *ApJ*, 399, 373
 Carnall, A. C., McLure, R. J., Dunlop, J. S., & Davé, R. 2018, *MNRAS*, 480, 4379
 Cayatte, V., Kotanyi, C., Balkowski, C., & van Gorkom, J. H. 1994, *AJ*, 107, 1003
 Chen, H.-W. 2017, in *Outskirts of Galaxies*, ed. J. H. Knapen, J. C. Lee, & A. Gil de Paz, Vol. 434 (Berlin: Springer), 291
 Chen, H.-W., Kennicutt, R. C., Jr., & Rauch, M. 2005, *ApJ*, 620, 703
 Chen, H.-W., & Lanzetta, K. M. 2003, *ApJ*, 597, 706
 Chen, H.-W., Zahedy, F. S., Boettcher, E., et al. 2020, *MNRAS*, 497, 498
 Chengalur, J. N., & Kanekar, N. 2002, *A&A*, 388, 383
 Cool, R. J., Eisenstein, D. J., Kochanek, C. S., et al. 2012, *ApJ*, 748, 10
 de Blok, W. J. G., Walter, F., Ferguson, A. M. N., et al. 2018, *ApJ*, 865, 26
 De Cia, A., Jenkins, E. B., Fox, A. J., et al. 2021, *Natur*, 597, 206
 De Cia, A., Ledoux, C., Mattsson, L., et al. 2016, *A&A*, 596, A97
 Dutta, R., Gupta, N., Srianand, R., & O'Meara, J. M. 2016, *MNRAS*, 456, 4209
 El-Badry, K., Bradford, J., Quataert, E., et al. 2018, *MNRAS*, 477, 1536
 Ferland, G. J., Chatzikos, M., Guzmán, F., et al. 2017, *RMxAA*, 53, 385
 Ferland, G. J., Porter, R. L., van Hoof, P. A. M., et al. 2013, *RMxAA*, 49, 137
 Fox, A. J., Wakker, B. P., Savage, B. D., et al. 2005, *ApJ*, 630, 332
 Gupta, N., Jagannathan, P., Srianand, R., et al. 2021, *ApJ*, 907, 11
 Gupta, N., Srianand, R., Baan, W., et al. 2016, in *MeerKAT Science: On the Pathway to the SKA*, Vol. 277 (Trieste: PoS), 14
 Gupta, N., Srianand, R., Farnes, J. S., et al. 2018, *MNRAS*, 476, 2432
 Haffert, S. Y., Bohn, A. J., de Boer, J., et al. 2019, *NatAs*, 3, 749
 Hunter, D. A., Ficut-Vicas, D., Ashley, T., et al. 2012, *AJ*, 144, 134
 Kanekar, N., Neeleman, M., Prochaska, J. X., & Ghosh, T. 2018, *MNRAS*, 473, L54
 Kanekar, N., Prochaska, J. X., Smette, A., et al. 2014, *MNRAS*, 438, 2131
 Kaur, B., Kanekar, N., Rafelski, M., et al. 2021, *ApJ*, 921, 68
 Kelson, D. D. 2003, *PASP*, 115, 688
 King, I. 1962, *AJ*, 67, 471
 Kovač, K., Oosterloo, T. A., & van der Hulst, J. M. 2009, *MNRAS*, 400, 743
 Krogager, J. K., Møller, P., Fynbo, J. P. U., & Noterdaeme, P. 2017, *MNRAS*, 469, 2959
 Lehner, N., Wotta, C. B., Howk, J. C., et al. 2019, *ApJ*, 887, 5
 Lelli, F., Verheijen, M., & Fraternali, F. 2014, *A&A*, 566, A71
 Liang, C. J., & Chen, H.-W. 2014, *MNRAS*, 445, 2061
 Maller, A. H., & Bullock, J. S. 2004, *MNRAS*, 355, 694
 Navarro, J. F., Frenk, C. S., & White, S. D. M. 1997, *ApJ*, 490, 493
 Neeleman, M., Kanekar, N., Prochaska, J. X., Rafelski, M. A., & Carilli, C. L. 2019, *ApJL*, 870, L19
 Neeleman, M., Prochaska, J. X., Ribaudo, J., et al. 2016, *ApJ*, 818, 113
 Osterbrock, D. E., & Ferland, G. J. 2006, *Astrophysics of Gaseous Nebulae and Active Galactic Nuclei* (2nd ed.; Sausalito, CA: University Science Books)
 Péroux, C., Quiret, S., Rahmani, H., et al. 2016, *MNRAS*, 457, 903
 Pettini, M., & Pagel, B. E. J. 2004, *MNRAS*, 348, L59
 Rao, S. M., Belfort-Mihalyi, M., Turnshek, D. A., et al. 2011, *MNRAS*, 416, 1215
 Read, J. I., Iorio, G., Agertz, O., & Fraternali, F. 2017, *MNRAS*, 467, 2019
 Salim, S., Boquien, M., & Lee, J. C. 2018, *ApJ*, 859, 11
 Savage, B. D., & Sembach, K. R. 1996, *ARA&A*, 34, 279
 Schulte-Ladbeck, R. E., König, B., Miller, C. J., et al. 2005, *ApJL*, 625, L79

- Schulte-Ladbeck, R. E., Rao, S. M., Drozdovsky, I. O., et al. 2004, *ApJ*, **600**, 613
- Serra, P., Westmeier, T., Giese, N., et al. 2015, *MNRAS*, **448**, 1922
- Srianand, R., Gupta, N., Petitjean, P., et al. 2012, *MNRAS*, **421**, 651
- Stevens, A. R. H., Diemer, B., Lagos, C. d. P., et al. 2019, *MNRAS*, **490**, 96
- Vale Asari, N., Couto, G. S., Cid Fernandes, R., et al. 2019, *MNRAS*, **489**, 4721
- Wang, J., Koribalski, B. S., Serra, P., et al. 2016, *MNRAS*, **460**, 2143
- Weilbacher, P. M., Streicher, O., Urrutia, T., et al. 2014, in ASP Conf. Ser. 485, *Astronomical Data Analysis Software and Systems XXIII*, ed. N. Manset & P. Forshay (San Francisco, CA: ASP), 451
- Westmeier, T., Kitaeff, S., Pallot, D., et al. 2021, *MNRAS*, **506**, 3962
- Wolfe, A. M., Gawiser, E., & Prochaska, J. X. 2005, *ARA&A*, **43**, 861
- Zahedy, F. S., Chen, H.-W., Cooper, T. M., et al. 2021, *MNRAS*, **506**, 877
- Zhang, K., Yan, R., Bundy, K., et al. 2017, *MNRAS*, **466**, 3217
- Zhao, D. H., Jing, Y. P., Mo, H. J., & Börner, G. 2009, *ApJ*, **707**, 354